Check for updates

ChemElectroChem

Research Article
doi.org/10.1002/celc.202400002

Chemistry Europe
European Chemical Societies Publishing

www.chemelectrochem.org

Enhanced Photoelectrochemical Activity Realized from WS_2 Thin Films Prepared by RF-Magnetron Sputtering for Water Splitting

Somnath Ladhane,[a] Shruti Shah,[a] Pratibha Shinde,[a] Ashvini Punde,[a] Ashish Waghmare,[a] Yogesh Hase,[a] Bharat R. Bade,[a] Vidya Doiphode,[a] Swati N. Rahane,[a] Dhanashri Kale,[a] Sachin R. Rondiya,[b] Mohit Prasad,[c] Shashikant P. Patole,*[d] and Sandesh R. Jadkar*[a]

We report the synthesis of tungsten sulfide (WS_2) films using RF-magnetron sputtering at different RF powers. X-ray diffraction (XRD) data confirm the hexagonal crystal structure of WS_2 with an average crystallite size of ~44.54 Å. With increased RF power, the preferred orientation of WS_2 crystallites shifts from (002) to (100). Linear sweep voltammetry (LSV) was used to assess the Photoelectrochemical (PEC) activity of WS_2 films. The film deposited at 150 W demonstrated the highest photocurrent density of 5.44 mA/cm^2. The 150 W film also showed a lower Tafel slope of ~0.374 V/decade, indicating superior PEC activity. Mott Schottky's (MS) analysis revealed a notable shift in the flat band potential towards the negative side, suggesting a shifting of the Fermi level towards the conduction band. WS_2 film grown at 150 W demonstrated a majority charge carrier density of 6.2×10^{21} cm^{-3} and a depletion layer width of 1.54 nm. The observed low charge transfer resistance of 155 Ω contributed to the enhanced PEC activity with a relaxation time constant of 37 ms. These properties suggest that WS_2 can be suitable for PEC water splitting.

Introduction

Transition metal dichalcogenides (TMDCs) are promising materials for optoelectronic applications. After the discovery of Graphene[1] in 2004, researchers developed more interest in this material due to its unique properties, such as high electrical conductivity of 1501.7 S/cm[2] and high charge carrier mobility of 10^6 cm^2/V-s at 2 K and 10^5 cm^2/V-s at room temperature[3] and extreme optical transparency (97.4%).[4] However, on the desk of optoelectronic applications, Graphene has limitations, such as its zero-band gap.[5] Like Graphene, layered TMDCs have earned substantial attention because of their advantageous electronic and photonic properties, such as narrow band gap of ~1.5 eV, high charge carrier mobility ~10^3 cm^{2}V^{-1}s^{-1} and relatively high optical sensitivity.[6,7] Due to these properties, numerous studies have been conducted on TMDCs in optoelectronic applications. These TMDC materials are chemically presented as MX_2, where M is a transition metal such as Mo, W, V, Nb, Ta, Ti, Zr, Hf, Tc, Re, and X is a chalcogenide element such as S, Se, and Te. They have sandwiched structures where transition metals are packed between two interlayer chalcogenide atoms. The chalcogenide atoms are bound with weak van der Waals forces and covalent bonds between transition metals to be exfoliated to form monolayer or few-layer structures.[8] The electrical properties of TMDCs strongly depend on morphology and synthesis protocol. They have an indirect bandgap for bulk and a direct bandgap for monolayers. Also, these 2D semiconducting materials are less toxic than graphene oxide.[9] Probing electrocatalytic activities in TMDCs, a new window of photonic materials with various optoelectronic applications such as hydrogen evolution reaction (HER),[10,11] humidity sensors,[12] solar cells,[13] etc., has emerged. Among all TMDCs, molybdenum disulfide (MoS_2) and tungsten disulfide (WS_2) have analogous structural, chemical, and physical properties such as band gap ~1–2 eV and relatively high absorption coefficient ~10^5 cm^{-1}[14,15] and hence gained the attention of the photovoltaic community.[6,16] Their bandgap potentially matches the solar energy spectrum. It shows high densities of active edge sites for photocatalysis.[17,18] These 2D semiconductors have many sites on the surface, which are helpful for photocatalytic activities. Also, both materials have layered structures with hydrogen binding energy close to Platinum (Pt)-group metals.[19] Therefore, they can be considered an alternative for Pt-group metals in hydrogen evolution.[20]

Recently, WS_2 has gained attention in the trade of thin film optoelectronic applications because of its properties.[21] It is an

[a] S. Ladhane, S. Shah, P. Shinde, A. Punde, Dr. A. Waghmare, Y. Hase, Dr. B. R. Bade, V. Doiphode, S. N. Rahane, D. Kale, Prof. S. R. Jadkar
Department of Physics, Savitribai Phule Pune University, Ganeshkhind Road, 411 007 Pune (India)
E-mail: sandesh@physics.unipune.ac.in

[b] Dr. S. R. Rondiya
Department of Materials Engineering, Indian Institute of Science, 560 012 Bengaluru (India)

[c] Dr. M. Prasad
Department of Applied Science and Humanities, Pimpri Chinchwad College of Engineering (PCCOE), Nigdi, 411 004 Pune (India)

[d] Dr. S. P. Patole
Department of Physics, Khalifa University of Science and Technology, 127788 Abu Dhabi (UAE)
E-mail: shashikant.patole@ku.ac.ae

© 2024 The Authors. ChemElectroChem published by Wiley-VCH GmbH. This is an open access article under the terms of the Creative Commons Attribution License, which permits use, distribution and reproduction in any medium, provided the original work is properly cited.

© 2024 The Authors. ChemElectroChem published by Wiley-VCH GmbH

Chemistry Europe
European Chemical Societies Publishing

efficient photocatalyst for hydrogen evolution reactions compared to MoS_2 as it has high electrical conductivity and active surface area, which is beneficial for photoelectrochemical (PEC) cells.[22] In addition, WS_2 is abundant, low-cost, and less hazardous for human beings than other TMDCs, so the development of WS_2 for optoelectronic applications is more reliable. It is thermally stable at high temperatures,[23] so it can be used as a lubricant,[24] and due to its chemical stability, it can serve as a protective barrier to avoid photo-corrosion of Si-like semiconductors.[25] Furthermore, due to the large size of the tungsten (W) atom, the structural properties of WS_2 can be tuned as per the need for optoelectronic applications.[26] Wang et al.[27] reported the synthesis of NiO@Ni/WS_2/CC heterostructure for water splitting with a current 10 mA/cm^2 at a cell voltage of 1.42 V. Similarly, *Zhang et al.*[28] synthesized WS_2 nano-sheets array on Co_3S_4 nanowires forming heterostructure on the carbon cloth towards water splitting reaction. *Yang et al.*[29] reported vertically aligned WS_2 nano-sheets for water-splitting applications. In recent years, the preparation of WS_2 films has been acquired by the mechanical exfoliation method,[30] chemical-based synthesis,[31] and chemical vapor deposition method (CVD).[32] Some researchers have utilized RF magnetron sputtering to deposit WS_2, exploring a range of deposition pressures and times[33] to observe the transition from 2D to 3D morphology. In another study, the RF power was varied during the deposition of MoS_2 to investigate its elemental composition and physiochemical properties.[34] Additionally, room temperature sputtering was employed to deposit WSe_2 for different deposition times to assess its impact on photocatalytic performance.[35] Moreover, MoS_2 was subjected to sputtering at various RF powers, and this technique was compared with thermal evaporation to analyze a distinctive deposition method for chalcogenides.[36] In chemical and mechanical exfoliation synthesis methods, it is hard to control the thickness and uniformity of the synthesized thin film. Also, in CVD, WS_2 thin film is ultra-thin and uniform on oxide substrates, but the surface contains many electrochemically inactive basal planes,[37] so WS_2 has less photoconductivity than MoS_2. The WS_2 can also be prepared by sulfurization of tungsten or tungsten oxide film.[38] However, controlling the sulfur content in this method is little tedious problematic. The preparation of WS_2 is also reported by the electrodeposition process,[39] but their tendency towards non-conformal growth on non-planar surfaces creates a disadvantage.

To overcome these limitations, RF-magnetron sputtering is the most suitable method to fabricate the thin film of WS_2. RF-sputtering is an ion-assisted plasma deposition process with which has many advantages, such as low cost, simple handling, high production speed, and scalability. The process parameters significantly influence the structural and chemical bonding of the material in RF-sputtering. As a result, optimizing the process parameters is critical to ensure ensuring successful material growth. Our study aims to investigate the structural, electrical, optical, and morphological properties of WS_2 thin films deposited via RF magnetron sputtering. Specifically, we varied the RF power to explore its impact on the films and evaluate their potential for use in photoelectrochemical water splitting. We found that the structural, electrical, optical, morphological, and PEC properties of WS_2 critically depend on RF power.

Experimental Section

Preparation of WS_2 thin films

Nanostructures of WS_2 were grown simultaneously on corning #7507 glass and fluorine-doped tin oxide (FTO) substrates using RF magnetron sputtering. The corning glass was pre-cleaned first by soap solution and then in piranha solution for 5 min and then dried with N_2 gas flow. For the deposition of WS_2 nanostructures, a 3-inch pure target of WS_2 (99.99%, Matsurf Technologies, USA) was used. The target-to-substrate distance is important in RF magnetron sputtering to eliminate pinholes. Considering the pinhole elimination strategy, the target-to-substrate distance was kept 12 cm throughout the deposition. The base pressure was adjusted for the deposition of WS_2 thin films ~3.0×10^{-5} Torr. The deposition pressure was held at 4 Pa, and the substrate temperature was maintained at 200 °C for better adhesion. The other deposition parameters are listed in Table 1.

After the deposition of WS_2, thin films were annealed at 400 °C for 1 hr in a tubular vacuum furnace for good crystallinity.

Thin film characterization

Structural properties of the as-deposited WS_2 thin film were investigated using a Bruker D8 Advance CuKα (λ = 0.15408 nm) diffractometer in the 2θ range of 10°–80°. A transmission electron microscope (TEM) (JEOL JEM-2100 PLUS, Japan), operated at a potential of 200 kV, was used to record TEM and selected area electron diffraction (SAED) patterns. Raman spectra were recorded using a Raman spectrometer (Renishaw InVia Raman spectroscopy) in the range 100–400 300–500 cm^{-1}, with a resolution of 1 cm^{-1}. A laser source with a wavelength of 532 nm with a laser power of 10 mW was used as an excitation source. The composition of elements was observed with an energy-dispersive spectrometer (EDS) (Oxford Instruments, USA). Nova NanoSEM 450 FESEM machine operated at 10 kV potential was used to capture cross-sectional views and surface morphology. The optical properties were examined using JASCO V-670, a UV-Visible spectrophotometer. X-ray photoemission spectroscopy (XPS) was used to investigate the chemical composition and oxidation state of W and S. For XPS Thermo Scientific, K-Alpha, UK machine with 0.1 eV resolution was used. PEC characterizations were performed using Metrohm Autolab Potentiostat: PGSTAT302N and a Xenon Lamp (PEC-L01) of 100 mW/cm^2 intensity.

Table 1. Process parameters used during the deposition of WS_2 thin film using RF-magnetron sputtering.

Process Parameters	Value/Condition
Base Pressure	3.0×10^{-5} Torr
Working Pressure	4 Pascal
Substrate Temperature	200 °C
RF Power	80–180 W
Post annealed Temperature	400 °C
Deposition time	20 min

© 2024 The Authors. ChemElectroChem published by Wiley-VCH GmbH

21960216, 0, Downloaded from https://chemistry-europe.onlinelibrary.wiley.com/doi/10.1002/celc.202400002 by The Librarian, Wiley Online Library on [22/03/2024]. See the Terms and Conditions (https://onlinelibrary.wiley.com/terms-and-conditions) on Wiley Online Library for rules of use; OA articles are governed by the applicable Creative Commons License

21960216, 0, Downloaded from https://chemistry-europe.onlinelibrary.wiley.com/doi/10.1002/celc.202400002 by The Librarian, Wiley Online Library on [22/03/2024]. See the Terms and Conditions (https://onlinelibrary.wiley.com/terms-and-conditions) on Wiley Online Library for rules of use; OA articles are governed by the applicable Creative Commons License

Photoelectrochemical (PEC) measurements

Photoelectrochemical characterizations were conducted in three-electrode cells where the WS_2 deposited on FTO was a working electrode, saturated calomel electrode (SCE) was a reference electrode, and Platinum was a counter electrode. The metal sulfides are stable in acidic electrolytes with a pH of less than 2. In this case, reducing agents HS^-, SO_3^{2-}, and $S_2O_3^{2-}$ have stabilized metal sulfide-based semiconductors. Therefore, we have used the 0.5 M H_2SO_4 aqueous solution as an electrolyte. The surface area of the working electrode was 1.0 cm^2. Chronoamperometry was performed by illumination of visible light having a power density of 100 mW/cm^2 at a bias of 0.5 V. Electrochemical impedance spectroscopy (EIS) was applied to determine the carrier charge transfer characteristics at the semiconductor-electrolyte interface. Linear sweep voltammetry (LSV) of the WS_2 thin films was recorded by the same potentiostat at a scan rate of 20 mV/s. The chronoamperometry curves were recorded at a bias of 0.5 V. The relationship between potential (vs. RHE) and potential (vs. SCE) is expressed as,[40]

$$V\ (\text{Vs.RHE}) = V\ (\text{Vs. SCE}) + (0.059 \times \text{pH}) + 0.244 \tag{1}$$

Where V (vs. SCE) is working potential.

Results and Discussion

X-ray Diffraction Analysis

Figure 1 shows the low-angle XRD of as-synthesized WS_2 thin films using the RF-magnetron sputtering method at different sputtering powers. The diffraction peak at 2θ ~13.90°, 33.24°, 58.88°, and 69.20° are assigned to (002), (100), (110), and (200) crystal planes of WS_2, respectively (JCPDS Card # 08-0237). These diffraction peaks are indexed to the hexagonal structure of WS_2 (P63/mmc space group, 2H-WS_2). No other impurity peaks were found in the XRD pattern, indicating the pure phase of WS_2. As seen, the WS_2 film deposited at 80 W has the preferred orientation of crystallites along the (002) plane. With an increase in RF power, the intensity of the (002) plane decreases, and at the same time, the intensity of the (100) diffraction plane increases. These results indicate that with increased RF power, the preferred orientation of WS_2 crystallites shifts from (002) to (100).

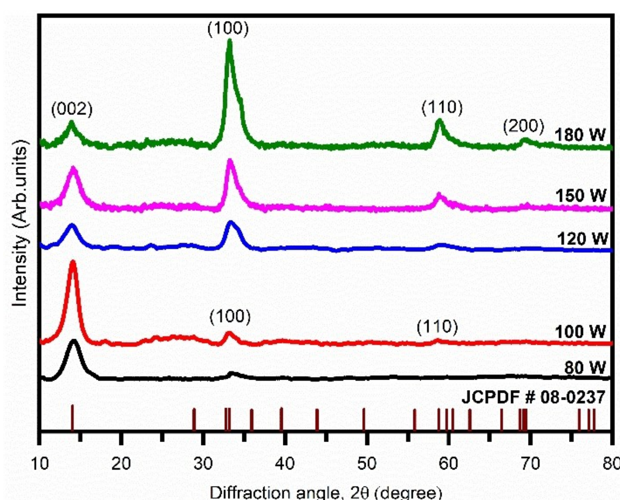

Figure 1. Low-angle XRD pattern of WS_2 films using RF-magnetron sputtering at different sputtering powers.

The interplanar spacing (d_{hkl}) of the WS_2 is estimated using Bragg's equation,

$$d_{hkl} = \frac{n\,\lambda}{2\ \text{Sin}(\theta)} \tag{2}$$

The calculated d_{100} and d_{002} values of WS_2 films ~0.27 nm and 0.6 nm, respectively, match the previously reported value,[41] which confirms the hexagonal WS_2 phase formation.

The lattice parameters of hexagonal WS_2 were calculated using the following equation,

$$\frac{1}{d_{hkl}^2} = \frac{4}{3}\left(\frac{h^2 + hk + k^2}{a^2}\right) + \frac{l^2}{c^2} \tag{3}$$

The calculated values of the lattice constants are a = 3.154, b = 3.154 Å, and c = 12.362 Å. The lattice values match the previously reported data.[42,43]

The peak's full width at half maximum (FWHM) is inversely proportional to the crystallite size (D_{hkl}) of the crystallites. It can be calculated by applying the *Debye-Scherrer* formula,[44]

$$D_{hkl} = \frac{0.9\,\lambda}{\beta_D\ \text{Cos}\theta} \tag{4}$$

Where θ is the angle between the incident and diffracted planes, β_D is the full width at half maximum (FWHM) of the peak in radians, and λ is the wavelength of the x-ray source.

The broadening of the diffraction peak is due to the micro strains present in the material. The lattice distortion and defect states are responsible for the microstrain. Thus, the total broadening is,[45]

$$\beta_{hkl} = \beta_D + \beta_\varepsilon \tag{5}$$

Here, β_{hkl} is the total broadening, and β_D and β_ε are the broadenings due to crystallite size and microstrain, respectively. The broadening and microstrain are related by,[46]

$$\varepsilon = \frac{\beta_\varepsilon}{4\ \text{Tan}\theta} \tag{6}$$

Where θ is the peak position, and ε is the microstrain. The broadening values can be calculated by rearranging eqs (4) and (6). Equation (5) becomes

$$\beta_{hkl} = \frac{K\,\lambda}{D_{hkl}\text{Cos}\theta} + 4\ \varepsilon\ \text{Tan}\theta \tag{7}$$

$$\beta_{hkl}\text{Cos}\theta = \frac{K\,\lambda}{D_{hkl}} + 4\ \varepsilon\ \text{Sin}\theta \tag{8}$$

© 2024 The Authors. ChemElectroChem published by Wiley-VCH GmbH

Chemistry Europe
European Chemical Societies Publishing

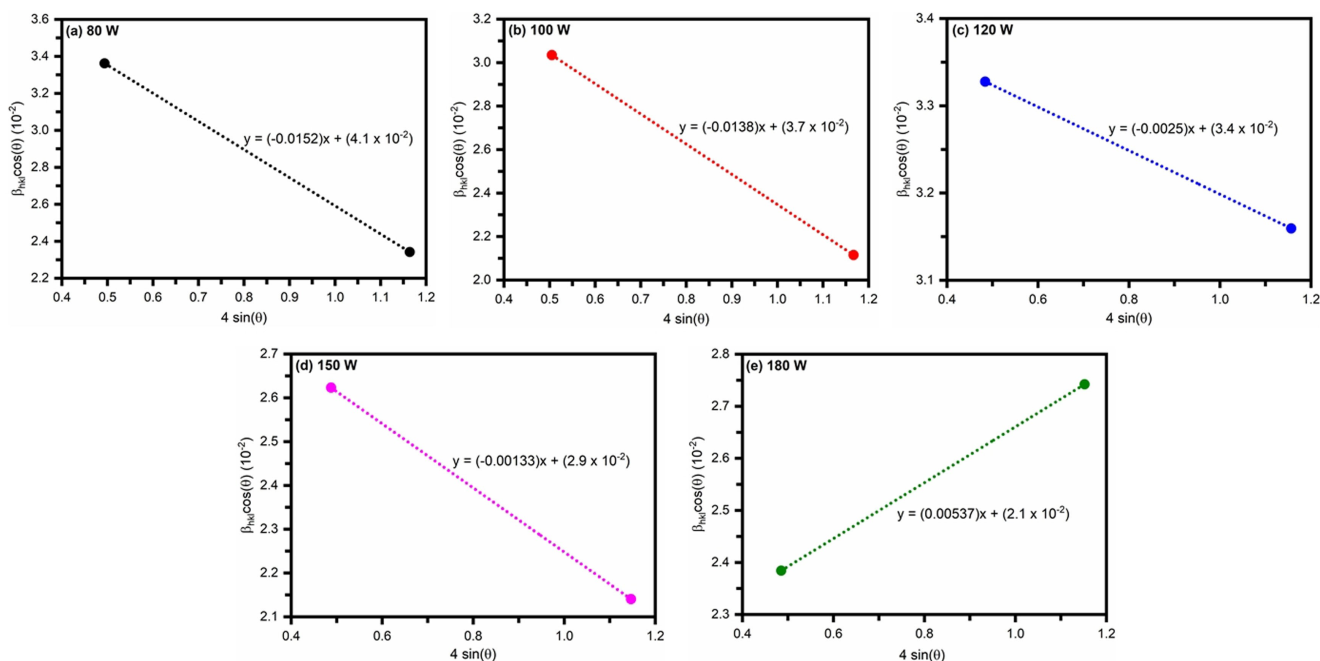

Figure 2. W-H plots for as-synthesized WS_2 films using RF-magnetron sputtering at different sputtering powers.

It represents a linear equation with $K\lambda/D_{hkl}$ as the intercept. Plotting a graph of β_{hkl} cosθ vs. 4 sinθ the slope and microstrain can be measured. The intercept value is inversely proportional to the crystallite size (D_{hkl}), and the slope is termed the microstrain. These plots are known as *Williamson-Hall* (W-H) plots. Figure 2 represents the W-H plots for WS_2 films prepared using the RF-magnetron sputtering method at different sputtering powers. Estimated values of crystallite size (D_{hkl}) and microstrain (ε) of all the variations are listed in Table 2. The calculated crystallite size found in the 33.68 Å to 65.25 Å over the entire range of RF power studied. The negative values of the microstrain revealed stacking faults in the WS_2 structure.[47] Negative values of W-H plots exhibit compressive strain in the materials, and the positive slope shows the tensile strain. As the RF power increases, the sputtered atoms are bombarded on the substrate with high energy. This highly energetic collision deforms the crystal structure, resulting in strain in the film. An increase in the strain value raises the dislocation density (δ).[48] It is the length of dislocation lines per unit volume of the crystal and was calculated using,[49]

$$\delta = \frac{n}{D_{hkl}^2} \tag{9}$$

Where n is the unity for the minimum number of densities. The values of dislocation density for all WS_2 are listed in Table 2.

Table 2. Calculated structural parameters of RF-magnetron sputtered WS_2 films at various RF powers.

RF Power (W)	Thickness (nm)	D_{hkl} (Å)	Microstrain ε (10^{-3})	$\delta\times10^{16}$ (lines/m^2)
80	65	33.68	−15.22	8.81
100	95	37.09	−13.89	7.26
120	130	40.18	−2.50	6.91
150	240	46.51	−1.33	4.62
180	270	65.25	5.73	2.34

Transmission Electron Microscopy Analysis

Further, to confirm the formation of WS_2, transmission electron microscopy (TEM) analysis was performed. Figures 3(a) and 3(b) depict the low and high-magnification bright-field TEM images of the WS_2, revealing the formation of numerous randomly oriented nanostructures such as nano ovals and nano-sheets. Figure 3(c) represents the magnified view of the selected area 'A' denoted by the dotted square in Figure 3(b). It shows that the interplanar spacing is ~0.27 nm, which agrees with the spacing of the (100) plane of hexagonal WS_2.[41] The observed results are consistent with XRD analysis (Figure 1) and confirm the formation of hexagonal WS_2 with randomly oriented nano ovals and nano-sheets. Figure 3(d) is the selected area electron diffraction (SAED) pattern of hexagonal WS_2. It shows the diffraction rings associated with the (002), (100) and (110) (200) planes of hexagonal WS_2.[50]

© 2024 The Authors. ChemElectroChem published by Wiley-VCH GmbH

21960216, 0, Downloaded from https://chemistry-europe.onlinelibrary.wiley.com/doi/10.1002/celc.202400002 by The Librarian, Wiley Online Library on [22/03/2024]. See the Terms and Conditions (https://onlinelibrary.wiley.com/terms-and-conditions) on Wiley Online Library for rules of use; OA articles are governed by the applicable Creative Commons License

Chemistry Europe
European Chemical Societies Publishing

21960216, 0, Downloaded from https://chemistry-europe.onlinelibrary.wiley.com/doi/10.1002/celc.202400002 by The Librarian, Wiley Online Library on [22/03/2024]. See the Terms and Conditions (https://onlinelibrary.wiley.com/terms-and-conditions) on Wiley Online Library for rules of use; OA articles are governed by the applicable Creative Commons License

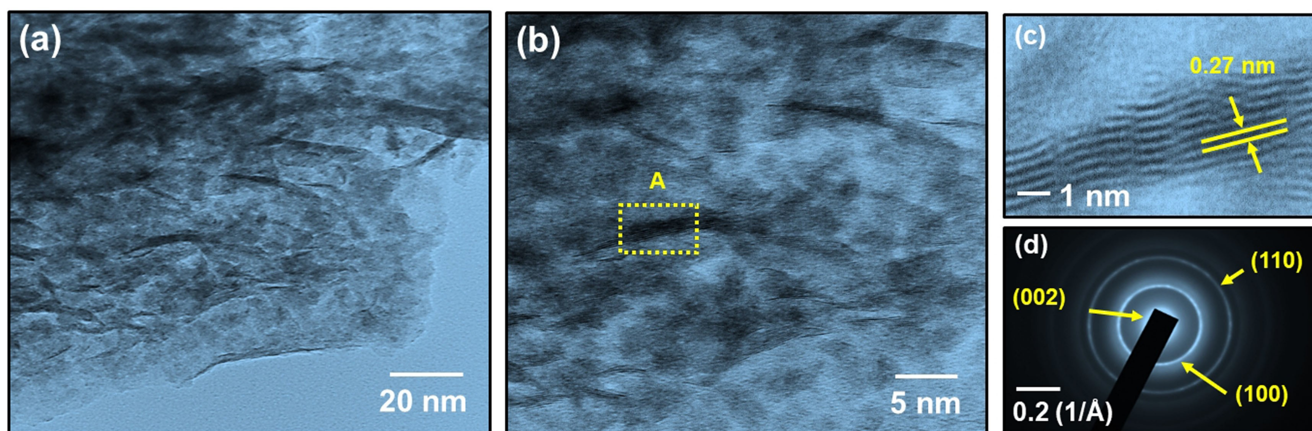

Figure 3. **(a)** and **(b)** Bright field TEM images of WS_2 film deposited at 150 W using RF magnetron sputtering, **(c)** Enlarged view of the marked area of 'A' in (b) showing the interplanar spacing between two lattice planes (~0.27 nm), and **(d)** SAED pattern.

Raman Spectroscopy Analysis

Active phonon modes and phase transition were examined by Raman spectroscopy. It is a powerful tool for characterizing materials' structural and vibrational properties. The intensity of the Raman peak is related to the strength of the interaction between the light and the material at that particular frequency.[51] The shape of the peak can provide information about the symmetry and anisotropy of the material. Figure 4 shows the Raman spectra of WS_2 films deposited at different RF power. It has been reported that for WS_2 compounds, there are generally four Raman-active modes viz; A_{1g}, E_{1g}, E^1_{2g}, and E^2_{2g} modes.[52] However, in the present work, A_{1g} and E^1_{2g} active modes were present. The absence of E^1_{2g} and E^2_{2g} modes can be due to the forbidden selection rule in the back-scattering geometry and the limited rejection against Rayleigh scattering. The Raman active A_{1g} E^1_{2g} mode occurs at ~351 $cm^{-1,}$ whereas the A_{1g} E^1_{2g} active mode occurs at ~419 cm^{-1}. The peak difference between these two peaks is 69 $cm^{-1,}$ which is in agreement agrees with the work reported by *Huang et al.*[53] and *Jeffery et al.*[54] No other impurity peaks were found, indicating the formation of a pure phase of WS_2.

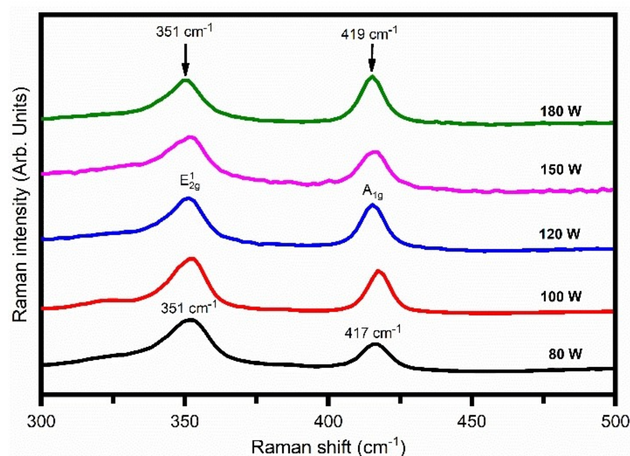

Figure 4. Raman spectra of WS_2 films deposited at different RF powers by the RF sputtering method.

X-ray photoelectron (XPS) analysis

XPS is a surface-sensitive analytical technique commonly used to characterize materials' chemical composition and electronic state. The XPS spectrum consists of peaks corresponding to the core-level binding energies of the different elements present in the film and the material's valence band. Figure 5(a) shows the

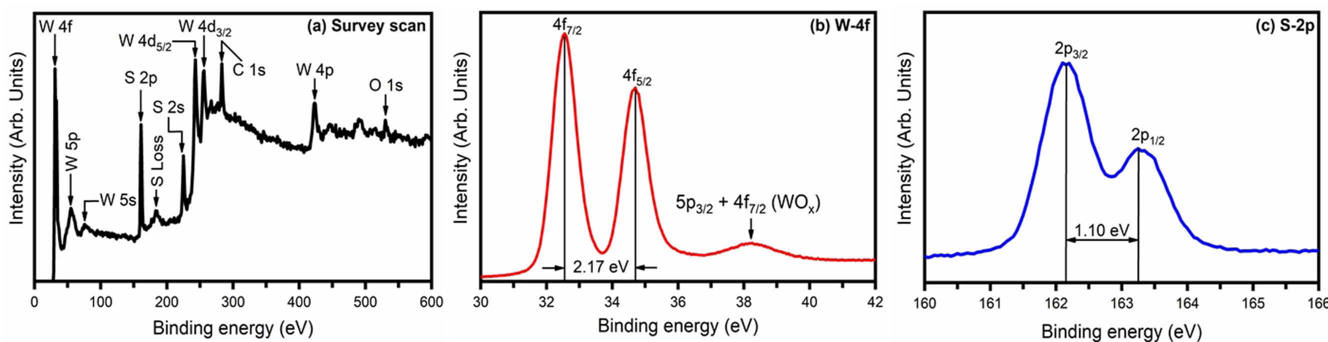

Figure 5. XPS spectra of WS_2 **(a)** Survey scan in the range 0– 800 600 eV **(b)** Narrow scan XPS spectra of W-4f and **(c)** Narrow scan XPS spectra of S-2p.

© 2024 The Authors. ChemElectroChem published by Wiley-VCH GmbH

21960216, 0, Downloaded from https://chemistry-europe.onlinelibrary.wiley.com/doi/10.1002/celc.202400002 by The Librarian, Wiley Online Library on [22/03/2024]. See the Terms and Conditions (https://onlinelibrary.wiley.com/terms-and-conditions) on Wiley Online Library for rules of use; OA articles are governed by the applicable Creative Commons License

survey spectrum of the WS_2 thin films, indicating the presence of tungsten (W), sulfur (S), oxygen (O), and carbon (C) elements in it. The XPS spectra were corrected using C 1s (284.6 eV) as a reference for correction. Figures 5(b) and (c) are the narrow scan XPS spectra for W-4f and S-2p elements, respectively. Figure 5(b) describes the narrow scan XPS spectra of the W 4f state of the WS_2 thin film grown at 150 W RF sputtering power. It shows two peaks, first at ~32.5 eV and second at ~34.6 eV, associated with W $4f_{7/2}$ and W $4f_{5/2}$, respectively, indicating that W exists mainly in the W^{4+} states of highly crystalline 2H-WS_2.[55] The energy separation between these two peaks was ~2.17 eV, a characteristic signal from the W^{4+} species due to spin-orbit interaction. The observed tiny peak at ~37.9 eV may be due to W $5p_{3/2}$ and W $4f_{5/2}$ in WOx species arising from surface oxidation. The peak observed at ~162.15 eV and ~163.3 eV for the same film is due to S $2p_{3/2}$ and S $2p_{1/2}$, respectively, with spin-orbit splitting separation of ~1.10 eV [Figure 5(c)]. It indicates the exitance of S^{2-} in the grown WS_2 thin films.[56] The data in the present work matches with the previously reported data in the literature,[57] confirming the formation of WS_2 thin films using the RF-magnetron sputtering method.

Morphological Surface Analysis

The surface morphology of as-deposited WS_2 thin films at different RF power is shown in Figure 6. The film has nano-flakes, nano-sheets, nano-oval chains, and nano-spheres-like morphology, confirming its critical dependency on RF power. At low RF powers (<150 W), the surface morphology of as-deposited WS_2 films is like nano-flakes and nano-sheets. Furthermore, as-deposited WS_2 thin films have porous micro-structures at low RF powers. At low RF power, the number of sputtered molecules arriving at the growing surface is less, resulting in porous morphology. As the RF power increases, the surface morphology of as-deposited WS_2 films becomes a nano-oval chain shape-like microstructure. The possible explanation for this could be the result of highly energetic atoms from the surface of the target bouncing bounce back and returning return to the substrate at high RF power.

Furthermore, as-deposited WS_2 thin films are compact and dense at high RF powers. All films are uniform and free from flaws and cracks. The WS_2 nano-flakes have an average length of hundreds of nanometers with an average thickness of ~20 nm. As power increases, enough atoms are ejected from the target and deposited on the substrate with the required formation energy, growing and the growth of the nano-sheets. As the morphology changes to sheets, the length increases to 200 nm, reducing the thickness to half of the nano-flakes. For chain-oval structures, sizes range from ~30–40 nm to that of nano-spheres ~60 nm. At the highest RF power, the oval chains merge into nano-spheres. These results confirm that RF power has a significant effect on grain size. The elemental compositions of the WS_2 films were determined using an Energy Dispersive X-ray Spectrometer (EDAX) coupled with a FESEM setup. Figure 7 shows the sulfur-to-tungsten (S/W) ratio variation as a function of RF sputtering power. The EDAX analysis of WS_2 films shows sulfur deficiency for all powers excluding 150 W. Consequently, the sulfur-to-tungsten ratio is nearly stoichiometric (1.97 : 1) for WS_2 film deposited at an RF power of 150 W. Due to sulfur deficiency, WS_2 grown at other RF powers has stiffness in the morphology. Thus, WS_2 film deposited at RF power of 150 W has a dense and compact structure due to the high energetic bombardment of atoms, which changes its morphology to ovular nano chains.

Optical analysis

The optical properties of as-deposited WS_2 films were studied using UV-Visible spectroscopy. Figure 8(a) shows the broad absorption spectra for WS_2 thin films in the 300–1400 nm range over the entire range of RF power varied. As seen, except for the WS_2 thin film deposited at an RF power of 100 W, the absorbance of the film increases with an increase in RF sputtering power. The observed red shift in the absorption can be due to the increase in crystallite size with an increase in RF power. The XRD analysis supports this conjuncture conjecture.

The absorption coefficient (α) is calculated using,

$$\alpha = 2.303 \times \frac{A}{t} \tag{10}$$

Where α is the absorption coefficient of the material in cm^{-1}, A is the absorbance, and t is the thickness of the film. The absorption coefficient of the material is the penetration depth of the material to its thickness, estimated to be ~10^4 cm^{-1}. The values of absorption coefficients for different RF powers are listed in Table 3. The optical band gap was calculated by using the absorption coefficient using the relation,[58]

$$\alpha h\nu = A(h\vartheta - E_g)^n \tag{11}$$

Where hν is the incident light energy in eV, E_g is the material's band gap in eV, and A is the constant. The value of n depends on the optical transition. It takes value 2 or 3 for indirect allowed or indirect forbidden transition, respectively, while for direct allowed and forbidden transition, it takes value 1/2 or 3/2, respectively. For indirect direct allowed transition, the optical band gap is obtained by extrapolating the tangential line to the photon energy (E = hυ) axis in the plot of $(\alpha h\upsilon)^{1/2}$ as a function of hυ (Tauc plot). Table 3 shows the calculated optical band gap values for different RF powers. The estimated values

Table 3. Calculated optical parameters of RF-magnetron sputtered WS_2 films at various RF powers.

RF Power (W)	Bandgap (eV)	Absorption coefficient $\times 10^4$ (cm^{-1})
80	1.07	2.30
100	1.48	1.80
120	1.37	3.1
150	1.30	6.20
180	0.87	2.40

© 2024 The Authors. ChemElectroChem published by Wiley-VCH GmbH

21960216, 0, Downloaded from https://chemistry-europe.onlinelibrary.wiley.com/doi/10.1002/celc.202400002 by The Librarian, Wiley Online Library on [22/03/2024]. See the Terms and Conditions (https://onlinelibrary.wiley.com/terms-and-conditions) on Wiley Online Library for rules of use; OA articles are governed by the applicable Creative Commons License

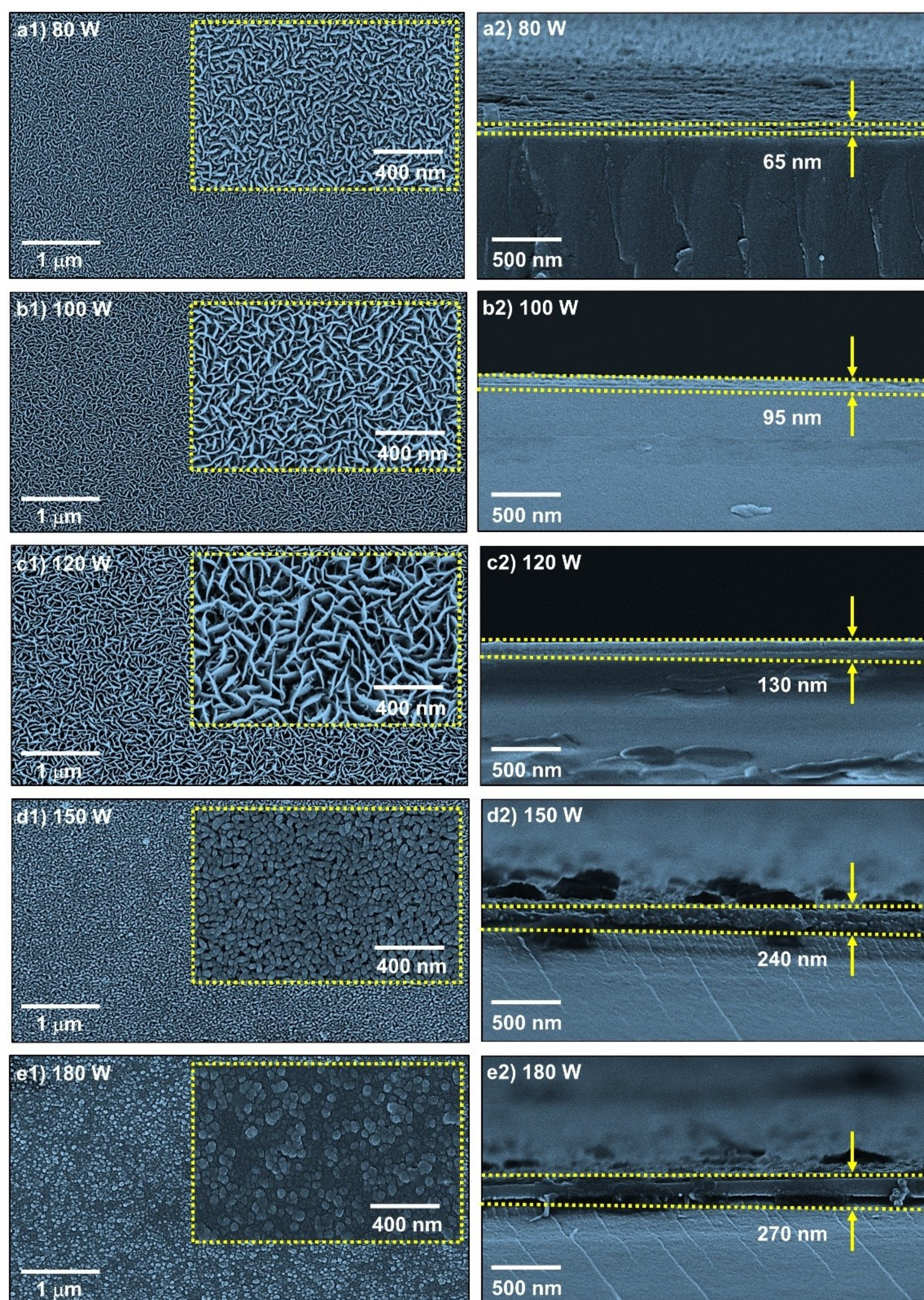

Figure 6. FESEM images and cross-section FESEM images of WS_2 thin films deposited by RF sputtering deposition technique at different deposition powers **a1)** and **a2)** 80 W, **b1)** and **b2)** 100 W, **c1)** and **c2)** 120 W, **d1)** and **d2)** 150 W, **e1)** and **e2)** 180 W respectively. inset in figures **a1)**, **b1**, **c1)**, **d1)** and **e1)** shows the corresponding magnified FESEM images.

of the optical band gap increased till 100 W RF power further decreased from 1.48 eV to 0.87 eV when RF power increased from 100 W to 180 W. The estimated values of optical band gaps were well-matched with previously reported data.[59]

Photoelectrochemical analysis

Linear sweep voltammetry (LSV) is a commonly used electrochemical technique for investigating the charge carrier characteristics at the semiconductor-electrolyte interface. When the voltage is applied to the WS_2 film, the electrons are excited to higher energy states, which increases the flow of electrons from the material to the electrode. LSV spectra were recorded by

© 2024 The Authors. ChemElectroChem published by Wiley-VCH GmbH

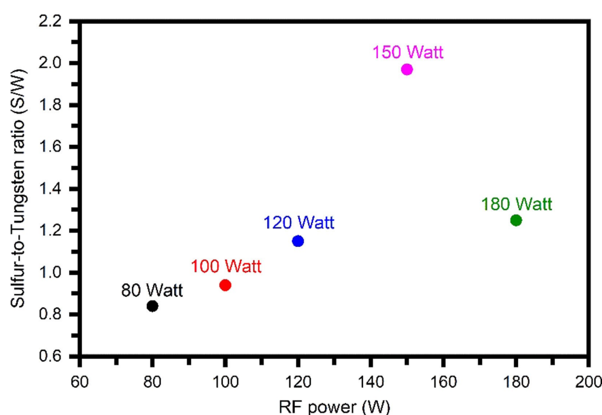

Figure 7. Variation of the sulfur-to-tungsten (S/W) ratio as a function of RF sputtering power.

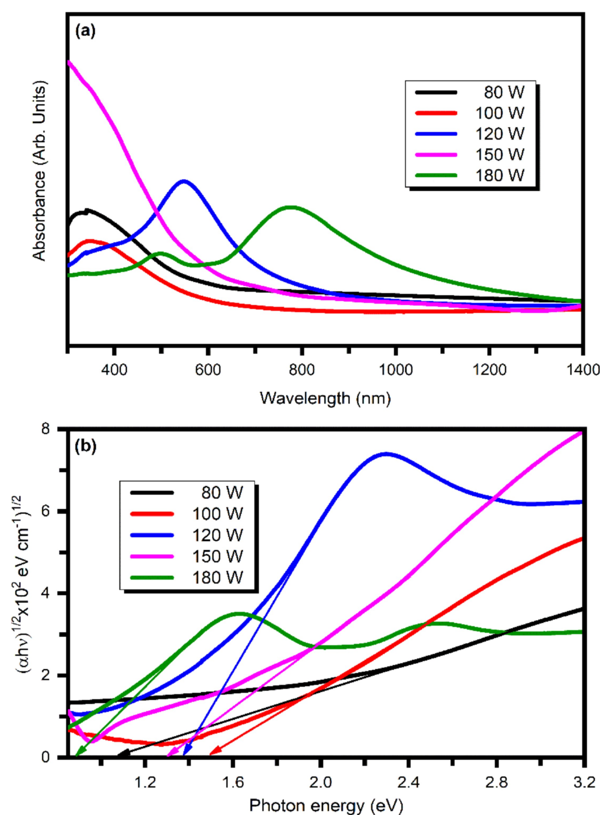

Figure 8. (a) UV-Visible absorption spectra of WS_2 films deposited at different RF powers **(b)** Tauc's plot of the same films.

applying a potential to the working electrode, which was anodically swept between −0.3 V to +0.7 V versus a saturated calomel electrode (SCE) under dark and illumination conditions. The LSV plot can also be interpreted mathematically using the *Butler-Volmer* equation, which relates the current density to the potential difference and the electrochemical properties of the material expressed as,[60]

$$j = j_0\left[e^{(\alpha_A \times f \times \eta)} - e^{(\alpha_c \times f \times \eta)}\right] \quad (12)$$

Where j_0 is the exchange current density, α_A is the anodic transfer coefficient and α_C is the cathodic transfer coefficient corresponding to multiple or single reactions, and η is over potential, which is given by,

$$\eta = V(\text{vs. RHE}) - E_{eq} \quad (13)$$

Here, V and E_{eq} are the operating potential and equilibrium potential, respectively, while

$$f = \frac{F}{RT} \quad (14)$$

Where F is Faraday's constant, R is the universal constant, and T is temperature.

When overpotential is high (>0.005 V), the Butler-Volmer equation becomes the Tafel equation,[61] which gives the relationship between the logarithm of current density and the overpotential as,

$$\log(j) = \log(j_0) + \left(\frac{\beta}{n}\right) \times \eta \times \text{Log}(j) \quad (15)$$

On the other hand, if the overpotential is low (<0.005 V), then the Butler-Volmer equation becomes,

$$j = j_0 \times n \times \eta \times f \quad (16)$$

Where j is the current density and j_0 is the exchange current density, β is the Tafel slope, n is the number of electrons transferred in the redox reaction, and η is the overpotential.

Figure 9(a) shows the Linear Sweep Voltammetry (LSV) plot for WS_2 thin films deposited at different RF powers. It is observed that 150 W is the optimized RF power for WS_2 growth, which shows the highest current density of 5.44 mA/cm^2. The FE-SEM surface morphology analysis further supports this. The improvement in the photocurrent density can be accredited to the increased surface area for film grown at 150 W, which absorbs many photons to generate electron-hole pairs. The Mott-Schottky and electrochemical impedance spectroscopy measurements also support the statement (discussed later). Overpotential is the excess potential required in an electrochemical reaction beyond the possibility of thermodynamic electrochemical reaction potential and can be calculated by LSV plot. This excess potential is necessary as many intermediates in the reaction require higher activation energy, particularly in catalytic processes. This results in an increased kinetic energy barrier that must be overcome. Therefore, to perform electrocatalytic water splitting, a potential greater than the equilibrium potential must be supplied to the system for accounting overpotential.[62] The relationship between overpotential and current density can be expressed as,

$$\eta = a + b\,\log(j) \quad (17)$$

Where b is the Tafel slope, and j is the current density.

© 2024 The Authors. ChemElectroChem published by Wiley-VCH GmbH

21960216, 0, Downloaded from https://chemistry-europe.onlinelibrary.wiley.com/doi/10.1002/celc.202400002 by The Librarian, Wiley Online Library on [22/03/2024]. See the Terms and Conditions (https://onlinelibrary.wiley.com/terms-and-conditions) on Wiley Online Library for rules of use; OA articles are governed by the applicable Creative Commons License

Chemistry Europe
European Chemical Societies Publishing

21960216, 0, Downloaded from https://chemistry-europe.onlinelibrary.wiley.com/doi/10.1002/celc.202400002 by The Librarian, Wiley Online Library on [22/03/2024]. See the Terms and Conditions (https://onlinelibrary.wiley.com/terms-and-conditions) on Wiley Online Library for rules of use; OA articles are governed by the applicable Creative Commons License

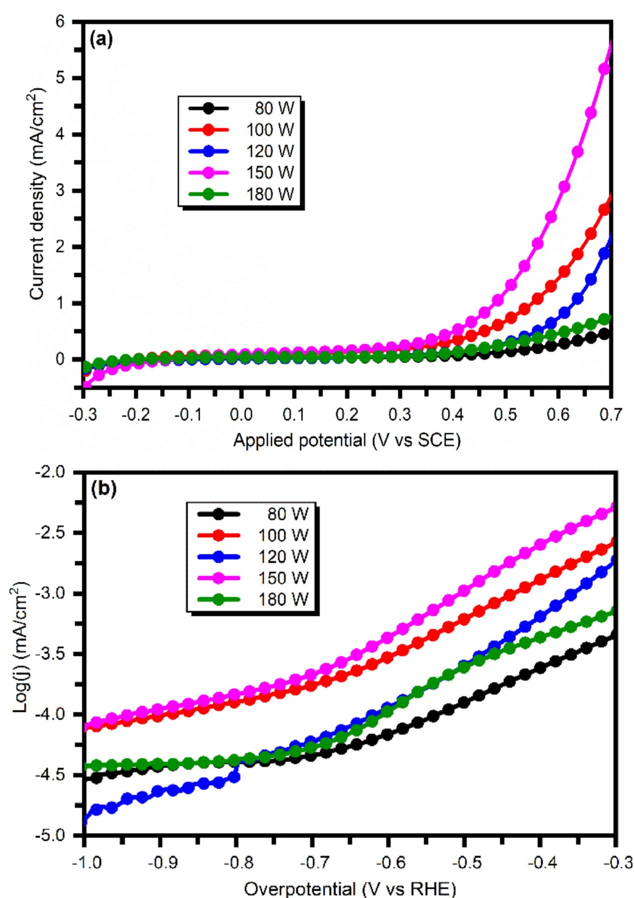

Figure 9. (**a**) Linear Sweep Voltammetry (LSV) measurements (**b**) Overpotential versus logarithmic current.

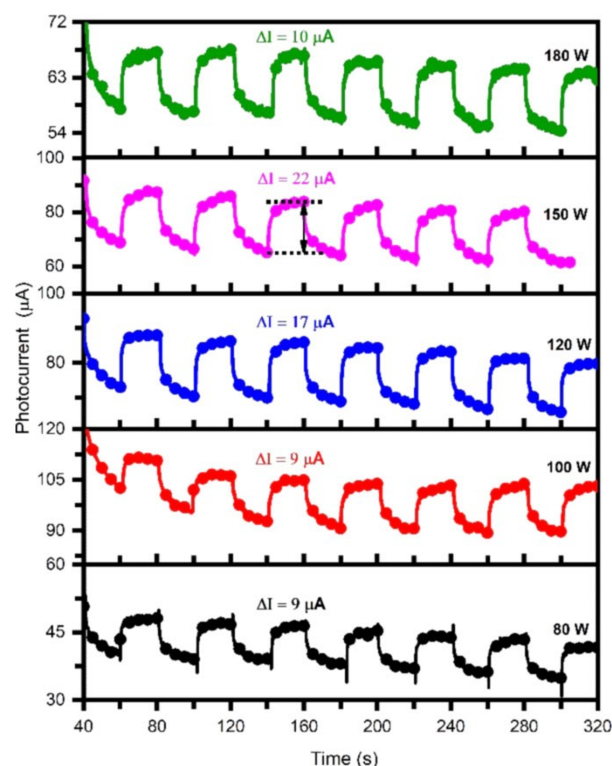

Figure 10. Current density versus time for WS_2 thin films deposited at different RF powers measured by applying a constant potential of +0.5 V at the working electrode with the chopping light conditions.

Figure 9(b) shows the plot of overpotential versus logarithmic current density. The Tafel slopes are 1.21 V/decade, 0.927 V/decade, 0.581 V/decade, 0.374 V/decade, and 4.41 V/decade for 80 W, 100 W, 120 W, 150 W, and 180 W, respectively. The Tafel slope needs to be low for better photoelectrochemical activities. Thus, WS_2 grown at 150 W RF power is suitable for better results.

Current density (J) versus time (t) was measured to investigate the photo response by applying a constant potential of +0.5 V at the working electrode with the chopping light conditions. Under light illumination, the WS_2 thin film grown at 150 W shows a photocurrent △I ~22 μA, the highest among all. This photo response is relatively high compared with the previously reported data.[63–65] The values for change in photocurrent for other power variations are shown in Figure 10. In these chronoamperometry profiles, a shallow slope was present that slowly decays the photocurrent, attributed to the slow recombination of charge carriers. The slow recombination happens due to a deficiency of S atoms in WS_2 thin films that generate trap states.[66]

Mott Schottky (MS) analysis is essential for investigating charge carrier transfer and separation mechanisms. It gives information about flat band potential and charges carrier density. The scans were carried out in the potential range of −0.8 V to +0.8 V at 1000 Hz. The MS plot illustrates the relationship between capacitance value and the potential difference between bulk semiconductors and electrolytes. By analyzing the MS plot, one can get information regarding the type of semiconductor and carrier concentration of a particular semiconductor.[67] The Mott-Schottky equation can be expressed as,

$$\frac{1}{C^2} = \frac{2}{\varepsilon_r \varepsilon_0 A^2 e\, N_D} \left(V - V_{FB} - \frac{KT}{e}\right) \quad (18)$$

Where C is the capacitance due to space charge, e is the charge on the electron, A is the surface area of the working electrode, ε_r is the relative permittivity of WS_2, ε_0 is the permittivity in vacuum (8.85×10^{-12} F/m), N_D is the density of donor charge carriers, V is applied potential, V_{FB} is the flat band potential, K is Boltzmann constant, and T is temperature. Charge carrier density was calculated from the slope of the plot of $1/C^2$ versus applied potential (V). Figure 11(a) shows the Mott-Schottky plot of grown WS_2 thin film at different RF power. The Mott-Schottky plot shows a positive slope, which indicates the n-type nature of WS_2 thin films. From the slope, the width of the depletion layer was calculated using,

$$\text{Slope} = \frac{2}{\varepsilon_r \varepsilon_0 A^2 e\, N_D} \quad (19)$$

© 2024 The Authors. ChemElectroChem published by Wiley-VCH GmbH

21960216, 0, Downloaded from https://chemistry-europe.onlinelibrary.wiley.com/doi/10.1002/celc.202400002 by The Librarian, Wiley Online Library on [22/03/2024]. See the Terms and Conditions (https://onlinelibrary.wiley.com/terms-and-conditions) on Wiley Online Library for rules of use; OA articles are governed by the applicable Creative Commons License

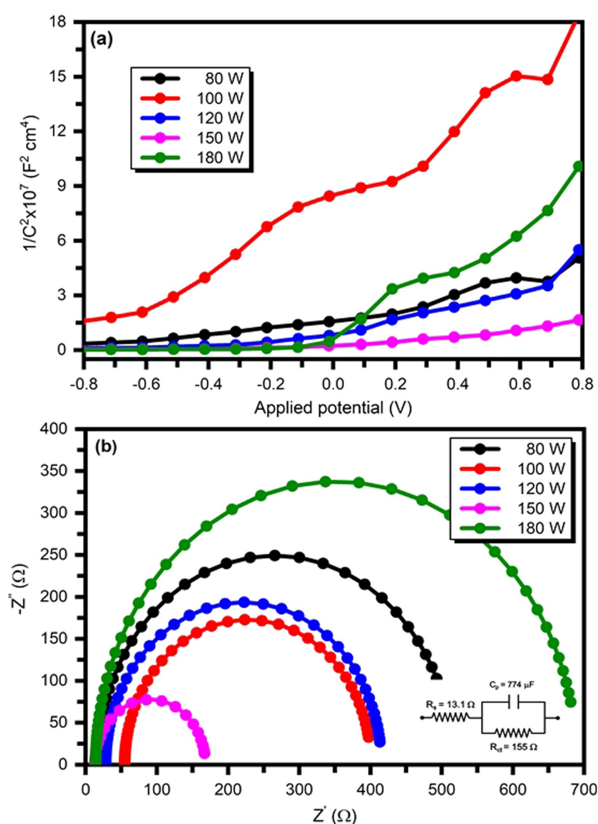

Figure 11. **(a)** Mott-Schottky plot **(b)** EIS spectra of as-deposited WS_2 thin film at different RF powers.

Table 4. Charge carrier density (N_D), flat band potential (V_{FB}), and depletion width (W_d) for WS_2 films deposited at different RF powers.

RF Power (W)	Charge carrier density (cm^{-3})	Flat band potential (V)	Depletion width (nm)
80	3.16×10^{21}	−0.19	3.54
100	1.12×10^{21}	−0.71	8.01
120	2.73×10^{21}	−0.42	3.45
150	6.20×10^{21}	−0.80	1.54
180	8.78×10^{20}	−0.12	5.01

$$W_d = \sqrt{\frac{2\varepsilon_r\varepsilon_0}{e\ N_D}(V - V_{FB})} \tag{20}$$

Where W_d is the width of the depletion layer. From the Mott-Schottky plot, flat band potential, the most important parameter for the working electrode (photoanode), was calculated. It gives the quantitative representation of the degree of band bending at the semiconductor-electrolyte interface.[68] When there is a greater degree of band bending, the interface will experience a reduction in electron-hole pair recombination, enhancing the efficiency of PEC and the excellent stability of the photoanodes. As a working electrode, when the WS_2 film is dipped into 0.5 M H_2SO_4 electrolyte solution, it consists of a sea of redox couple like O_2 and H_2O, and charge carrier transfer is carried out between the working electrode and electrolyte solution to attain equilibrium condition. When charged particles in an electrolyte solution interact with charged particles in the working electrode, it causes charges to build up and a depletion width to form. The flat band potential for film grown at 150 W shifted towards the more negative side, indicating the shifting of the Fermi level towards the conduction band. Lower depletion width provides an easy way to transfer the photogenerated charge carriers. Table 4 shows the values of Charge carrier density (N_D), flat band potential (V_{FB}), and depletion width (W_d) for WS_2 films deposited at different RF powers.

Electrochemical impedance spectroscopy was executed under light illumination conditions to understand the qualitative insights of charge transfer kinetics in bulk and at the semiconductor-electrolyte interface. The EIS measurements were carried out in the 0.01 Hz to 100 kHz frequency range by applying the constant potential of 0.5 V (Nyquist plot). The conductivity and charge transfer resistance can be determined by analyzing the Nyquist plot. The data obtained from EIS for WS_2 films was fitted by a simulated Randles equivalent electric circuit shown in the inset of Figure 11(b), and the fitted parameters are tabulated in Table 5. At high frequencies, information about the influence of the bulk matrix on the electrochemical reaction can be obtained, while at low frequencies, measurement provides information about the double-layer capacitance.[69] From the Nyquist plot, it is observed that the WS_2 film grown at 180 W shows the semicircle of greater radius, indicating high charge carrier resistance with low charge carrier separation efficiency. However, the WS_2 film deposited for RF power at 150 W shows the smallest semicircle radius, indicating the lowest charge transfer resistance and high charge carrier separation efficiency.

The Bode phase is a graphical representation of the phase response of a system as a function of frequency. Figure 12(a) shows the bode plot for RF power-varied WS_2 films. At higher frequencies, the phase shift becomes more significant, indicating a more prolonged time needed to respond to input signal

Table 5. Values for charge transfer resistance (R_{ct}), capacitance (C_p), relaxation frequency, relaxation time constant (τ_e), and diffusion length (L_d).

RF power (W)	Charge transfer resistance (Ω)	Capacitance (F)	Relaxation frequency (Hz)	Relaxation time constant (ms)	Diffusion length (mm)
80	499	3.35×10^{-4}	5.72	27.83	5.67
100	346	4.40×10^{-4}	4.32	36.86	6.62
120	387	2.89×10^{-4}	5.73	27.78	5.75
150	155	7.74×10^{-4}	4.30	37.03	6.64
180	675	2.64×10^{-4}	7.56	21.06	5.01

© 2024 The Authors. ChemElectroChem published by Wiley-VCH GmbH

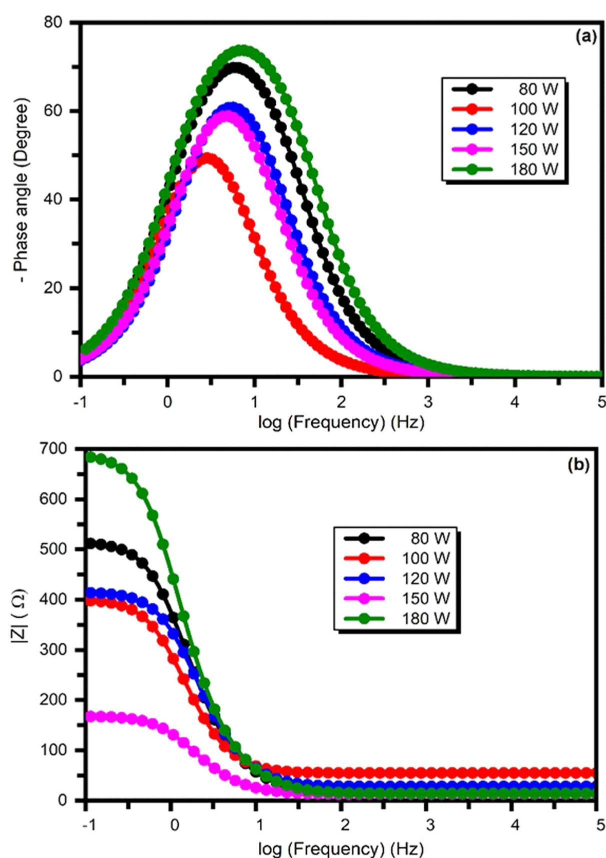

Figure 12. **(a)** Bode phase plot and **(b)** Bode modulus plot of as-deposited WS_2 thin film at different RF powers.

changes. On the other hand, the slight phase shift at low frequencies means a quick responding nature.

The majority charge carrier lifetime can be calculated by using a Bode plot. The equation for relaxation time constant can be expressed as,

$$\tau_e = \frac{1}{2\pi f_{max}} \tag{21}$$

Where f_{max} is the peak frequency at the maximum phase, and τ_e is the relaxation time. The majority charge carrier lifetime for all WS_2 films is listed in Table 5. The relaxation time constant (τ_e) is higher, which means the recombination rate of photogenerated charge carriers is low. Among all the WS_2 films, nanostructures grown at 150 W show a greater relaxation time constant, which implies a lower rate of charge carrier recombination.

Figure 12(b) shows the bode modulus plot for the WS_2 films deposited at different RF powers. The modulus plot gives information about the change in charge transfer resistance concerning frequency. It was observed from Figure 12(b) that thin film grown at 150 W has very low impedance for low frequency but as deposition power increases, the impedance increases. The WS_2 thin film grown at 150 W performs better throughout the application and agrees well with the structural and optical properties.

Diffusion length is vital in analyzing interfacial processes, such as photoelectrochemical activities. EIS measurements can also be used to determine the diffusion length. This method assumes that the relaxation time constant is equivalent to the time holes take to oxidize a water molecule.[70] The diffusion length can be expressed as,[71]

$$L_d = 2\sqrt{(D \times \tau_e)} \tag{22}$$

Where D is the diffusion coefficient of the photogenerated hole.

The calculated diffusion length is greater than the thickness of the films. It includes diffusion within the solid catalysts and at the interface, suggesting that the transport of minority charge carriers outside the electrochemical interface is most probable. When the diffusion length is longer than the depletion width, the minority carriers can diffuse far away from the p-n junction before recombining, resulting in higher device efficiency. It is desirable in photoelectrochemical activities, where a long diffusion length is essential for efficient carrier collection and conversion of light into electricity.

Table 6 gives the different TMDC materials, their preparative methods, and morphology for PEC water splitting. The results obtained in the present study are also included in the table for comparison. The RF-magnetron sputtering-grown WS_2 exhibited enhanced PEC activities for water splitting compared with those prepared by different methods and morphologies. Thus, the present work provides a straightforward and effective approach for constructing and designing WS_2 photoanodes with high PEC performance for water splitting.

Table 6. Comparison of PEC water splitting performance of various TMDCs with different preparation methods and morphology.

Material	Preparative method	Morphology	Outcomes	Reference
γ-In_2Se_3	RF sputtering	Nano grains	0.9 mA m^{-2}	[72]
MoS_2/WSe_2	Liquid-phase exfoliation and vacuum filtration	Nanosheets	0.4 mA cm^{-2} (V Vs SCE)	[73]
MoS_2	Chemical Exfoliation	Rolled up edges	0.2 μA cm^{-2} (0 V)	[74]
γ-In_2Se_3	Hot injection method	Clustered nanoflakes	88.5 μA cm^{-2}	[75]
N-doped ZnO	Hydrothermal	Nanowires	400 μA cm^{-2} (1 V vs SCE)	[76]
WS_2	**RF sputtering**	**Nanosheets and Nano ovals**	**5 mA cm^{-2} (V Vs SCE)**	**Present Work**

© 2024 The Authors. ChemElectroChem published by Wiley-VCH GmbH

21960216, 0, Downloaded from https://chemistry-europe.onlinelibrary.wiley.com/doi/10.1002/celc.202400002 by The Librarian, Wiley Online Library on [22/03/2024]. See the Terms and Conditions (https://onlinelibrary.wiley.com/terms-and-conditions) on Wiley Online Library for rules of use; OA articles are governed by the applicable Creative Commons License

21960216, 0, Downloaded from https://chemistry-europe.onlinelibrary.wiley.com/doi/10.1002/celc.202400002 by The Librarian, Wiley Online Library on [22/03/2024]. See the Terms and Conditions (https://onlinelibrary.wiley.com/terms-and-conditions) on Wiley Online Library for rules of use; OA articles are governed by the applicable Creative Commons License

Conclusions

We had synthesized WS_2 films using RF magnetron sputtering at different RF powers for PEC water splitting. We found that RF power directly impacts the structural, optical, morphological, and PEC properties of WS_2 films. XRD and Raman spectroscopy confirmed the formation of the pure and hexagonal 2H phase of WS_2, with an average crystallite size of ~44.54 Å. Furthermore, as the RF power increased, the preferred orientation of WS_2 crystallites shifted from (002) to (100). TEM analysis further confirms and reveals that the interlayer spacing around 0.27 nm corresponding to (100) plane XPS analysis revealed spin-orbit splitting values of ~2.17 eV for W and ~1.10 eV for S, providing further evidence of the presence of the 2H phase of WS_2. FESEM analysis demonstrated that the surface morphology of WS_2 was significantly influenced by the RF power, resulting in various nanostructures such as nano-flakes, nano-sheets, nano-oval chains, and nano-sphere-like formations. The film exhibited broad absorption with a band gap ranging from 0.87 eV to 1.48 eV and an average absorption coefficient of ~10^4 cm^{-1}, suggesting the suitability of WS_2 for optoelectronic applications. The LSV analysis revealed that the WS_2 film deposited at 150 W has the highest photocurrent density of ~5.44 mA/cm^2. Additionally, it exhibited a lower Tafel slope of ~0.374 V/decade, indicating superior PEC activity. Mott-Schottky analysis showed a shift of the flat band potential towards the negative side, suggesting a shift of the Fermi level towards the conduction band. The WS_2 film grown at 150 W had a charge carrier density of ~6.2×10^{21} cm^{-3} and a depletion layer width of ~1.54 nm. The enhanced PEC activity observed in the 150 W film was attributed to its low charge transfer resistance (~155 Ω) and a relaxation time constant of ~37.03 ms. These results suggest that WS_2 films, particularly those grown at 150 W, hold promise for PEC water-splitting applications.

Author Contributions

Somnath Ladhane: Methodology, Formal analysis, Investigation, Data curation, Writing-original draft; **Shruti Shah**: Methodology, Validation, Formal analysis, Investigation; **Pratibha Shinde**: Conceptualization, Validation, Formal analysis, Investigation; **Ashvini Punde**: Methodology, Validation, Formal analysis, Investigation; **Ashish Waghmare**: Methodology, Formal analysis, Investigation, Data curation; **Yogesh Hase**: Methodology, Conceptualization, Validation, Formal analysis, Investigation; **Bharat Bade**: Conceptualization, Validation, Formal analysis, Investigation; **Vidya Doiphode**: Methodology, Validation, Formal analysis, Investigation; **Swati Rahane**: Data curation, Formal analysis, Investigation; **Dhanashri Kale**: Data curation, Formal analysis, Investigation; **Sachin Rondiya**: Formal analysis, Data curation; **Mohit Prasad**: Data curation, Writing-Review, and Editing; **Shashikant P. Patole**: Writing-Review, Editing, Supervision, Funding acquisition; **Sandesh Jadkar**: Visualization, Writing-Review, Editing, Supervision, Funding acquisition

Acknowledgements

Shruti Shah, Vidya Doiphode, Pratibha Shinde, Ashish Waghmare, Yogesh Hase, and Bharat Bade are grateful to the Ministry of New and Renewable Energy (MNRE), Government of India New Delhi, for the National Renewable Energy (NRE) fellowship and financial assistance. Ashvini Punde is thankful to the Mahatma Jyotiba Phule Research and Training Institute (MAHA-JYOTI), Government of Maharashtra, for the Mahatma Jyotiba Phule Research Fellowship (MJPRF). Swati Rahane is thankful for the research fellowship to the Chhatrapati Shahu Maharaj Research, Training and Human Development Institute (SARTHI), Government of Maharashtra. Dhanashri Kale is grateful to the Department of Science and Technology, Government of India, New Delhi, for the financial support under the Innovation in Science Pursuit for Inspired Research (INSPIRE) fellowship. Finally, Shashikant P. Patole would like to thank Khalifa University for its financial support through the internal fund for high-quality publications.

Conflict of Interests

The authors declare no conflict of interest.

Data Availability Statement

The datasets used and analyzed during the current study are available from the corresponding author upon reasonable request.

Keywords: WS_2 thin films · RF-magnetron sputtering · Nanostructures · Photoelectrochemical activity

[1] K. S. Novoselov, A. K. Geim, S. V. Morozov, D. Jiang, Y. Zhang, S. V. Dubonos, I. V. Grigorieva, A. A. Firsov, *Science* **2004**, *306*, 666–669.
[2] Z. Wang, Y. Zhang, P. Tang, Z. Deng, P. He, M. J. Chen, Z. Z. Yu, H. B. Zhang, *Carbon* **2003**, *203*, 886–894.
[3] K. Geim, K. S. Novoselov, *Nat. Mater.* **2007**, *6*, 183–191.
[4] P. Blake, P. D. Brimicombe, R. R. Nair, T. J. Booth, D. Jiang, F. Schedin, L. A. Ponomarenko, S. V. Morozov, H. F. Gleeson, E. W. Hill, A. K. Geim, K. S. Novoselov, *Nano Lett.* **2008**, *8*, 1704–1708.
[5] E. Mazarei, C. Penschke, P. Saalfrank, *ACS Omega* **2023**, *8*, 22026–22041.
[6] Q. H. Wang, K. K. Zadeh, A. Kis, J. N. Coleman, M. S. Strano, *Nat. Nanotechnol.* **2012**, *7*, 699–712.
[7] X. Xu, W. Yao, D. Xiao, T. F. Heinz, *Nat. Phys.* **2014**, *10*, 343.
[8] X. Duan, C. Wang, A. Pan, R. Yu, X. Duan, *Chem. Soc. Rev.* **2015**, *44*, 8859–8876.
[9] J. Low, S. Cao, J. Yu, S. Wageh, *Chem. Commun.* **2014**, *50*, 10768–10777.
[10] L. Wang, Y. Zhang, C. Gu, H. Yu, Y. Zhuang, Z. Zhua, *Nano Res.* **2023**, https://doi.org/10.1007/s12274-023-6374-7.
[11] L. Xie, L. Wang, X. Liu, W. Zhao, S. Liu, X. Huang, Q. Zhao, *Angew. Chem. Int. Ed.* **2023**, *63*, e202316306.
[12] H. Song, X. Zhu, E. Yang, Z. Han, *IEEE Trans. Electron Devices* **2023**, *70*, 1849–1853.
[13] T. Iqbal, S. Ahsan, F. Saeed, M. S. Sultan, A. A. AlObaid, I. Warad, A. Masood, *Plasmonics* **2023**, *18*, 1255–1265.
[14] R. Ganatra, Q. Zhang, *ACS Nano.* **2014**, *8*, 4074–4099.
[15] S. Chen, C. Zheng, M. S. Fuhrer, J. Yan, *Nano Lett.* **2015**, *15*, 2526–2532.
[16] W. Zhao, Z. Ghorannevis, K. K. Amara, J. R. Pang, Mi. Toh, X. Zhang, C. Kloc, P. H. Tane, G. Eda, *Nanoscale* **2013**, *5*, 9677–9683.

© 2024 The Authors. ChemElectroChem published by Wiley-VCH GmbH

Chemistry Europe
European Chemical Societies Publishing

[17] K. C. Kwon, S. Choi, K. Hong, C. W. Moon, Y. S. Shim, D. H. Kim, T. Kim, W. Sohn, J. M. Jeon, C. H. Lee, K. T. Nam, S. Han, S. Y. Kim, H. W. Jang, *Energy Environ. Sci.* **2016**, *9*, 2240–2248.
[18] Z. Cheng, Z. Wang, T. A. Shifa, F. Wang, X. Zhan, K. Xu, Q. Liu, J. He, *Appl. Phys. Lett.* **2015**, *107*, 223902.
[19] S. Trasatti, *J. Chem. Soc. Faraday Trans.* **1995**, *91*, 3311–3325.
[20] K. C. Pham, Y. H. Chang, D. S. McPhail, C. Mattevi, A. T. S. Wee, D. H. C. Chua, *ACS Appl. Mater. Interfaces* **2016**, *8*, 5961–5971.
[21] M. Rafiq, N. Amin, H. F. Alharbi, M. Luqman, A. Ayob, Y. S. Alharthi, N. H. Alharthi, B. Bais, M. Akhtaruzzaman, *Sci. Rep.* **2020**, *10*, 771.
[22] T. Y. Chen, Y. H. Chang, C. L. Hsu, K. H. Wei, C. Y. Chiang, L. J. Li, *Int. J. Hydrogen Energy* **2013**, *38*, 12302–12309.
[23] W. A. Brainard, *NASA, Washington* **1969**, NASA TN D-5141.
[24] S. V. Prasad, N. T. McDevitt, J. S. Zabinski, *Wear* **2000**, *237*,186–196.
[25] L. Zeng, Y. Liu, S. Lin, W. Qarony, L. Tao, Y. Chai, X. Zhang, S. P. Lau, Y. H. Tsang, *Sol. Energy Mater. Sol. Cells* **2018**, *174*, 300–306.
[26] A. Eftekhari, *J. Mater. Chem. A* **2017**, *5*, 18299–18325.
[27] D. Wang, Q. Li, C. Han, Z. Xing, X. Yang, *ACS Cent. Sci.* **2018**, *4*, 112–119.
[28] T. Zhang, F. Song, Y. Wang, J. Yuan, L. Niu, A. Wang, K. Fang, *Electrochim. Acta* **2022**, *404*, 139648.
[29] Y. Yang, H. Fei, G. Ruan, Y. Li, J. M. Tour, *Adv. Funct. Mater.* **2015**, *25*, 6199–6204.
[30] C. Awasthi, S. S. Islam, *Mater. Sci. Semicond. Process.* **2023**, *162*, 107554.
[31] M. S. Barbosa, D. N. O. Barbosa, R. A. da Silva, M. O. Orlandi, *Chem. Phys. Lett.* **2023**, *812*, 140269.
[32] J. Yan, Y. Huang, Z. Cao, Y. An, *Vacuum* **2023**, *208*, 111725.
[33] Y. Koçak, E. Gür, *ACS Appl. Mater. Interfaces* **2020** *12(13)*, 15785–15792.
[34] J. Park, Y. C. Kang, *Bull. Korean Chem. Soc.* **2016**, *37*, 1326–1330.
[35] J. Nam, M. Jang, H. Jang, W. Park, X. Wang, S. Choi, B. Cho, Y. Kim, J. Yang, *J. Energy Chem.* **2019**.
[36] A. T. Borgogoi, D. J. Borah, A. T. T. Mostako, *Physica B: Condensed Matter* **2023**, *660*, 414896.
[37] Y. Yang, H. Fei, G. Ruan, C. Xiang, J. M. Tour, *Adv. Mater.* **2014**, *26*, 8163–8168.
[38] P. Gultom, J.-Y. Chiang, T.-T. Huang, J.-C. Lee, S.-H. Su, J.-C. Andrew Huang, *Nanomaterials* **2023**, *13*, 1276.
[39] L. Fan, I. I. Suni, *J. Electrochem. Soc.* **2017**, *164*, D681.
[40] T. Zahra, K. S. Ahmad, A. G. Thomas, C. Zequine, R. K. Gupta, M. A. Malik, M. Sohail, *RSC Adv.* **2020**, *10*, 29961.
[41] C. S. Rout, P. D. Joshi, R. V. Kashid, D. S. Joag, M. A. More, A. J. Simbeck, M. Washington, S. K. Nayak, D. J. Late, *Sci. Rep.* **2013**, *3*, 3282.
[42] J. Yan, S. Lian, Z. Cao, Y. Du, P. Wu, H. Sun, Y. An, *Vacuum* **2023**, *207*, 111564.
[43] A. Roy, P. Kalita, B. Mondal, *J. Mater. Sci. Mater. Electron.* **2023**, *34*, 224.
[44] Cullity, S. Stock, *Elements of X-ray diffraction*, Princeton Hall, 3rd Ed^{n}, **2001**.
[45] S. Öz, J. C. Hebig, E. Jung, T. Singh, A. Lepcha, S. Olthof, F. Jan, Y. Gao, R. German, P. H. M.v. Loosdrecht, K. Meerholz, T. Kirchartz, S. Mathur, *Sol. Energy Mater. Sol. Cells.* **2016**, *158*, 195–201.
[46] D. Tiwari, D. Alibhai, D. J. Fermin, *ACS Energy Lett.* **2018**, *3*, 1882–1886.
[47] K. R. Beyerlein, R. L. Snyder, M. Li, P. Scardi, *Philos. Mag.* **2010**, 3891–3905.
[48] S. Chander, & M. S. Dhaka, *J. Mater. Sci. Mater. Electron.* **2016**, *27*, 11961; M. S. Dhaka, *J. Mater. Sci. Mater. Electron.* **2016**, *27*, 11961.
[49] S. Kite, P. Chate, K. Garadkar, D. Sathe *J. Mater. Sci. Mater. Electron.* **2017**, *28*, 16148–54.
[50] L. Zeng, L. Tao, C. Tang, B. Zhou, H. Long, Y. Chai, S. P. Lau, Y. H. Tsang, *Sci. Rep.* **2016** *6*, 20343.
[51] D. C.Harris, M. D. Bertolucci, *Oxford University Press*: *New York, NY*, *USA*, **1978**.
[52] A. Molina-Sanchez, L. Wirtz, *Phys. Rev. B* **2011**, *84*, 155413.
[53] F. Huang, J. Jian, R. Wu, *J. Mater. Sci.* **2016**, *51*, 10160–10165.
[54] A. A. Jeffery, C. Nethravathi, R. Michael, *J. Phys. Chem. C.* **2014**, *118(2)*, 1386–1396.
[55] R. Morrish, T. Haak, C. A. Wolden, *Chem. Mater.* **2014**, *36*, 3986–3992.
[56] T. A. J. Loh, D. H. C. Chua, A. T. S. Wee, *Sci. Rep.* **2015**, *5*, 18116.
[57] R. Scarfiello, E. Mazzotta, D. Altamura, C. Nobile, R. Mastria, S. Rella, C. Giannini, P. D. Cozzoli, A. Rizzo, C. Malitesta, *Nanomaterials* **2021**, *11*, 1969.
[58] S. L. Patel, S. Chander, A. Purohit, M. D. Kannan, M. S. Dhaka, *J. Phys. Chem. Solids* **2018**, *123*, 216–222.
[59] E. Singh, K. S. Kim, G. Y. Yeom, H. S. Nalwa, *RSC Adv.* **2017**, *7(45)*, 28234–28290.
[60] G. Inzelt, *J. Solid State Electrochem.* **2011**.
[61] A. M. Arts, *Electronic Theses and Dissertations Paper.* **2021**, 3903.
[62] H. S. Casalongue, S. Kaya, V. Viswanathan, D. J. Miller, D. Friebel, H. A. Hansen, J. K. Nørskov, A. Nilsson, H. Ogasawara, *Nat. Commun.* **2013**, *4*, 2817.
[63] M. Zirak, M. Zhao, O. Moradlou, M. Samadi, N. Sarikhani, Q. Wang, H.-L. Zhang, A. Moshfegh, *Sol. Energy Mater. Sol. Cells* **2015**, *141*, 260–269.
[64] Y. Zhong, Y. Shao, F. Ma, Y. Wu, B. Huang, X. Hao, *Nano Energy* **2017**, *31*, 84–89.
[65] M. S. Akple, J. Low, S. Wageh, A. A. Al-Ghamdi, J. Yu, J. Zhang, *Appl. Surf. Sci.* **2015**, *358*, 196–203.
[66] R. Cheng, S. Jiang, Y. Chen, Y. Liu, N. Weiss, H. C. Cheng, H. Wu, Y. Huang, X. Duan, *Nat. Commun.* **2014**, *5*, 5143.
[67] J. Su, L. Guo, N.Z Bao, C. A. Grimes, *Nano Lett.* **2011**, *11*, 1928–1933.
[68] K. Gelderman, L. Lee, S. Donne, *J. Chem. Educ.* **2007**, *84*, 685.
[69] A. Fujishima, K. Honda, *Nature* **1972**, *238*, 37–38.
[70] S. Kumar, S. Ahirwar, A. K. Satpati, *RSC Adv.* **2019**, *9*, 41368.
[71] H. Liu, C. Wang, Z. Zuo, D. Liu, J. Luo, *Adv. Mater.* **2020**, *32*, 1906540.
[72] A. Waghmare, V. Sharma, P. Shinde, S. Shah, A. Punde, Y. Hase, B. Bade, V. Doiphode, S. Rahane, S. Ladhane, M. Prasad, S. Rondiya, S. Jadkar, *J. Mater. Sci. Mater. Electron.* **2023** *34*, 1139.
[73] K. Si, J. Ma, C. Lu, Y. Zhou, C. He, D. Yang, X. Wang, X. Xu, *Appl. Surf. Sci.* **2020**, *507*, 145082.
[74] R. K. Joshi, S. Shukla, S. Saxena, G.-H. Lee, V. Sahajwalla, S. Alwarappan, *AIP Adv.* **2016**, *6*, 015315.
[75] G. M. Kumar, J. R. Kumar, P. Ilanchezhiyan, M. Paulraj, H. C. Jeon, D. Y. Kim, T. W. Kang, *J. Mater. Res. Technol.* **2020** *9(6)*, 12318–12327.
[76] Z. Kang, H. Si, S. Zhang, J. Wu, Y. Sun, Q. Liao, Z. Zhang, Y. Zhang, *Adv. Funct. Mater.* **2019**, *29*, 1808032.

Manuscript received: January 1, 2024
Revised manuscript received: January 18, 2024
Version of record online: ■■, ■■

© 2024 The Authors. ChemElectroChem published by Wiley-VCH GmbH

21960216, 0, Downloaded from https://chemistry-europe.onlinelibrary.wiley.com/doi/10.1002/celc.202400002 by The Librarian, Wiley Online Library on [22/03/2024]. See the Terms and Conditions (https://onlinelibrary.wiley.com/terms-and-conditions) on Wiley Online Library for rules of use; OA articles are governed by the applicable Creative Commons License

RESEARCH ARTICLE

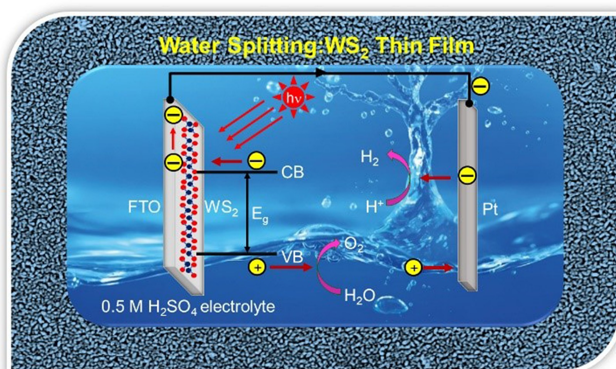

WS_2 for PEC splitting: In this article, we study the properties of WS_2 thin films deposited using RF magnetron sputtering. We focus on structural, electrical, optical, and morphological properties in view of their use for PEC water splitting. By varying the RF power, we investigate its impact on the nanostructures and assess their potential for use in photoelectrochemical water splitting.

S. Ladhane, S. Shah, P. Shinde, A. Punde, Dr. A. Waghmare, Y. Hase, Dr. B. R. Bade, V. Doiphode, S. N. Rahane, D. Kale, Dr. S. R. Rondiya, Dr. M. Prasad, Dr. S. P. Patole, Prof. S. R. Jadkar**

1 – 14

Enhanced Photoelectrochemical Activity Realized from WS_2 Thin Films Prepared by RF-Magnetron Sputtering for Water Splitting

21960216, 0, Downloaded from https://chemistry-europe.onlinelibrary.wiley.com/doi/10.1002/celc.202400002 by The Librarian, Wiley Online Library on [22/03/2024]. See the Terms and Conditions (https://onlinelibrary.wiley.com/terms-and-conditions) on Wiley Online Library for rules of use; OA articles are governed by the applicable Creative Commons License